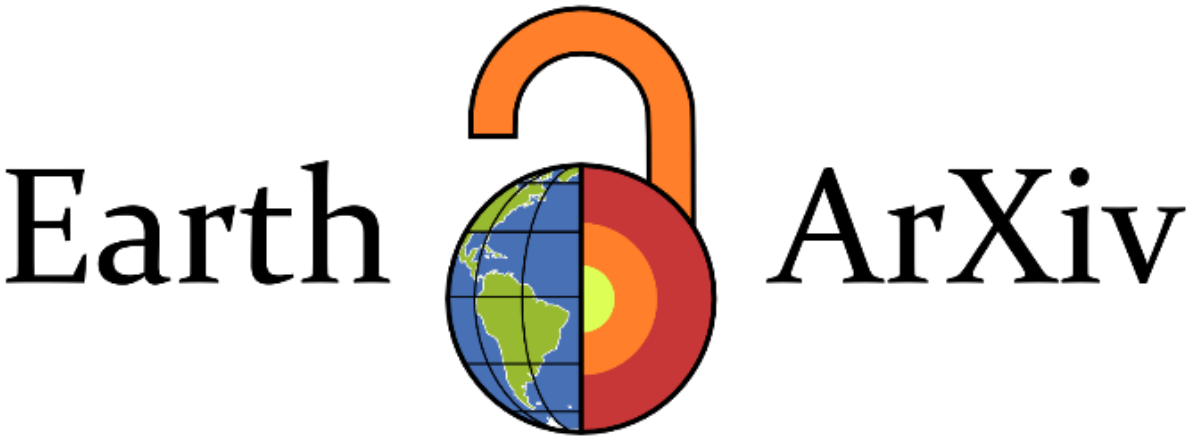

Massive High-Fidelity Focal Mechanisms Reveal Detailed Structure of Re-Activated Faults During Hydraulic Fracturing in Western Canada

Jiachen Hu[1], Yunfeng Chen[1], Hongyu Yu[1], Fangxue Zhang[1], Xing Li[2], Yangkang Chen[2]

[1]Key Laboratory of Geoscience Big Data and Deep Resource of Zhejiang Province, School of Earth Sciences, Zhejiang University, Hangzhou, China
[2]Bureau of Economic Geology, Jackson School of Geosciences, The University of Texas at Austin, Austin, TX, USA

Key Points:

- Micro-EQpolarity model achieves 99.20% accuracy for P-wave polarity determination, resolving 2519 microseismic focal mechanisms
- NS-Fault reactivation is controlled by higher friction and enhanced cohesion, possibly triggered by stress transfer and pore pressure
- NE-Fault activation follows fluid diffusion through low-dip fault conduits, with fluid migration patterns revealed by massive focal mechanisms

Corresponding author: Yunfeng Chen, yunfeng_chen@zju.edu.cn

Abstract

Microseismic focal mechanism solutions (FMSs) are essential for understanding reservoir stress changes and rock fracturing during hydraulic fracturing. While machine learning has shown strong performance in seismic data processing tasks, including phase picking and magnitude estimation, as well as identifying P-wave first-motion polarity for moderate to large earthquakes to invert FMSs, its application to microseismic events remains limited. This limitation arises from the distinct characteristics of microseismicity, such as lower signal-to-noise ratios (SNR) and different rupture mechanisms, which challenge the effectiveness of existing polarity pickers. At the same time, the increasing deployment of dense seismic arrays has generated vast amounts of data, creating both the need and opportunity to develop AI models specifically tailored to microseismic events. In response to the challenges of determining the P-wave first-motion polarity for microseismic events, we propose Micro-EQpolarity, a fine-tuned model based on the EQpolarity framework. The model combines convolutional blocks for feature extraction, transformer blocks for feature enhancement, and an MLP network for classification. Utilizing transfer learning, the model is pre-trained on the Southern California Seismic Network (SCSN) dataset and fine-tuned with 19,724 manually selected waveforms from the Tony Creek Dual Microseismic Experiment (ToC2ME) dataset, achieving an accuracy of 99.20%. Applied to seismic data from Western Canada, Micro-EQpolarity successfully inverted 2,519 high-quality focal mechanism solutions, creating a comprehensive catalog that extends analysis to events with magnitudes as low as -1.4. The model identified four distinct FMS types, revealing fine-scale fault structures and detailed patterns of fault reactivation. These findings provide new insights into fault reactivation mechanisms in the NS-Fault cluster and fluid diffusion processes in the NE-Fault cluster. In the NS-Fault cluster, our analysis reveals two possible reactivation mechanisms: higher friction coefficients and enhanced cohesion, with fault reactivation driven by the combined effects of Coulomb static stress and pore-fluid pressure. In the NE-Fault cluster, two-stage hydraulic fracturing facilitated fluid propagation, initially reaching the southwestern part of Fault 1 before spreading to Faults 2-6, with Fault 3 acting as a "transfer station" directing fluid diffusion both eastward and westward through low-dip fault conduits.

Plain Language Summary

Hydraulic fracturing operations can trigger small underground earthquakes called microseismic events. Understanding these tiny earthquakes is crucial for monitoring reservoir changes and optimizing extraction processes, but existing methods designed for larger earthquakes perform poorly on microseismic data due to their lower signal-to-noise ratios and different characteristics. We developed Micro-EQpolarity, an artificial intelligence model specifically designed for microseismic events, achieving over 99% accuracy. Applied to Western Canada microseismic data, our model successfully analyzed 2,519 earthquake mechanisms, including events with negative magnitudes. Our analysis revealed two main fault systems with distinct behaviors. In the NS-Fault area, some faults required extra pressure from both injected fluids and stress from larger earthquakes to activate because they had rougher surfaces and stronger rock bonds. In the NE-Fault area, we traced how injected fluids moved through underground pathways, spreading from fault to fault over time.

1 Introduction

Microseismic events, often characterized by their small magnitudes and even negative moment magnitudes, are commonly induced by industrial activities such as hydraulic fracturing or fluid flow within reservoirs. The focal mechanism solutions (FMSs) of these events play a crucial role in understanding subsurface stress changes and fracture behaviors during hydraulic stimulation, which are central to the success of operations in the

oil and gas industry. Specifically, FMSs provide critical insights into the principal stress axes, thereby enabling the analysis of fault orientations, slip behaviors (e.g., strike-slip, normal, or reverse faulting), and their relationship to stress perturbations induced by industrial activities (Deichmann & Ernst, 2009; Zoback, 1992; McKenzie, 1969). By mapping the orientation and dynamics of induced fractures through these analyses, FMSs help operators optimize hydraulic fracturing processes, ensure caprock integrity during in situ heavy-oil extraction, and advance technologies such as carbon capture and storage (van der Baan et al., 2013; Jia et al., 2018). At the same time, dense seismic arrays have been widely utilized to monitor microseismic events, providing critical insights into seismic risks and potential hazards associated with unconventional shale gas and oil development (Trow et al., 2018; Nyffenegger et al., 2022; Meng & Ben-Zion, 2017). Nevertheless, the rapid deployment of dense arrays and the growth of real-time seismology technologies have produced vast amounts of seismic data, presenting significant challenges for routine earthquake cataloging and the rapid determination of focal mechanisms.

Focal mechanism inversion methods can generally be divided into two categories: P-wave first-motion-based methods and waveform-based methods. While waveform-based methods eliminate the need for manual phase picking, they are highly sensitive to noise and computationally demanding, particularly when simulating high-frequency seismograms or solving the wave equation numerically (Zhao et al., 2023; Chen et al., 2024; Kim et al., 2011). These challenges are further amplified for small-magnitude earthquakes, which require highly accurate local velocity models and precise simulation of high-frequency waveforms. In contrast, P-wave first-motion-based methods are computationally more efficient, making them more practical for large datasets and routine processing. However, they are not without limitations, as they can be prone to errors caused by polarity picking and noise interference, while the manual process of picking P-wave first-motion polarity is both time-consuming and labor-intensive. These challenges highlight the need for a highly reliable automated P-wave first-motion polarity picker for microseismic events monitored by dense arrays.

In recent years, machine learning has been increasingly applied to various aspects of automated seismic data processing, including tasks such as seismic data denoising (Zhu et al., 2019; Saad et al., 2025; C. Li et al., 2025), earthquake detection (Perol et al., 2018; Saad & Chen, 2020; Saad et al., 2022; Mousavi et al., 2020), seismic phase picking (Ross, Meier, Hauksson, & Heaton, 2018; J. Wang et al., 2019; Zhou et al., 2019; Mousavi et al., 2020; Saad & Chen, 2021; Saad et al., 2023), phase association (Ross, Meier, Hauksson, & Heaton, 2018; Zhu et al., 2025; Ross et al., 2019), earthquake location (Van den Ende & Ampuero, 2020; M. Zhang et al., 2022), magnitude estimation (Mousavi & Beroza, 2020; Saad et al., 2022), focal mechanism determination (Kuang et al., 2021; Tian et al., 2025; P. Wang et al., 2024), and earthquake early warning systems (X. Zhang et al., 2021). Machine learning has been increasingly utilized for identifying P-wave first-motion polarity (e.g., (Ross, Meier, & Hauksson, 2018; Uchide, 2020; Chen et al., 2024; Zhao et al., 2023; Han et al., 2025), often demonstrating strong performance for moderate to large-magnitude earthquakes. For instance, a convolutional neural networks (CNN) was trained with millions of manually labeled seismograms recorded in Southern California (Ross, Meier, & Hauksson, 2018) . Based on this work, Cheng et al. (2023) developed a workflow, CNN_SoCal, to identify changes in focal mechanism properties induced by large mainshocks, such as the 2010 Mw7.2 El Mayor-Cucapah and 2019 Mw7.1 Ridgecrest earthquakes. Compared to moderate sized earthquakes, microseismic events exhibit distinct characteristics, including smaller magnitudes, higher frequencies, lower signal-to-noise ratios, shorter wavelengths, and shorter durations (Kamei et al., 2015). These differences can significantly affect the performance of existing polarity pickers, often resulting in inaccuracies when determining the P-wave first-motion polarity for microseismic events.

To address the challenges of accurately determining the P-wave first-motion polarity for microseismic events, this study introduces Micro-EQpolarity, a fine-tuned model

based on the EQpolarity framework (Chen et al., 2024), specifically designed for microseismic analysis. Importantly, we adopt a transfer learning strategy to fine-tune the base model to improve its performance in microseismic polarity determination task. Transfer learning is an efficient training approach that initializes new models with pre-trained parameters and adapts them through fine-tuning, offering faster and more efficient training compared to starting from scratch (Lapins et al., 2021; Yu & Ma, 2021). This approach has been successfully applied to various seismological tasks, including adapting PhaseNet (Zhu & Beroza, 2018) from natural to hydraulic fracturing earthquakes (Chai et al., 2020), transferring EQTransformer (Mousavi et al., 2020) from land to ocean bottom seismic data (Niksejel & Zhang, 2024), and applying EQCCT (Saad et al., 2023) to Texas earthquake data under low SNR conditions (Saad et al., 2024). For microseismic polarity determination specifically, transfer learning provides an ideal solution by leveraging abundant labeled data from moderate-to-large earthquakes to overcome the scarcity of high-quality microseismic datasets, while ensuring cross-regional usability and an optimal accuracy-efficiency balance. By utilizing data pre-trained from the Southern California Seismic Network (SCSN) (Southern California Earthquake Data Center, 2013), we fine-tune our model using data from the Tony Creek Dual Microseismic Experiment (ToC2ME) (Eaton et al., 2018). The ToC2ME is a field program that employed a diverse array of sensors to record a hydraulic fracturing completion program at a four-well pad located west of Fox Creek, Alberta. Notably, the array provided exceptional azimuthal coverage, enabling a significantly lower magnitude of completeness compared to regional monitoring networks (H. Zhang et al., 2019), which makes it an excellent dataset for training and testing machine learning models.

This excellent dataset has greatly improved our understanding of various aspects of induced seismicity. However, several key aspects remain to be further explored from previous work, which a comprehensive focal mechanism catalog can help advance. First, regarding fault system structural complexity, previous studies have progressively utilized improved earthquake catalogs to reveal increasingly detailed fault architectures. Starting with 4,083 events, Eaton et al. (2018) identified strike-slip dominated clusters with north-south lineaments and N30°E trending features deviating from regional stress orientations. Igonin et al. (2021) expanded to 18,472 events, revealing preexisting fracture networks facilitating fluid pressure communication. To resolve finer-scale fault structures, focal mechanisms provide crucial insights into fault geometry and slip characteristics, enabling construction of comprehensive three-dimensional fault network models. Second, concerning triggering mechanism uncertainty, our understanding of the relative importance and interactions among various processes—pore-fluid pressure diffusion, poroelastic stress changes, Coulomb static stress transfer, and aseismic slip—requires further improvement. Igonin et al. (2021) demonstrated fault reactivation initiated by fluid pressure transfer along fracture networks, while F. Zhang et al. (2022) further revealed that the same fault may be dominated by different mechanisms during early injection phases (pore-fluid pressure diffusion) versus later stages (Coulomb stress transfer), or their combination. Third, regarding intrinsic fault system properties, parameters such as cohesion, friction coefficients, and the strike deviation from the SH_{max} orientation play crucial roles in determining reactivation thresholds. How these fault properties influence reactivation processes represents a fundamental yet underexplored research question. For the second and third challenges, a comprehensive focal mechanism catalog could provide essential information including background stress regime characterization and spatiotemporal progression patterns for different fault types, significantly advancing our understanding of reactivation mechanisms.

Addressing these fundamental questions requires high-resolution earthquake catalogs and improved focal mechanism solutions (FMSs). Leveraging the workflow outlined in Section 2.2, which incorporates a two-stage transfer learning strategy—pre-trained on the SCSN dataset and fine-tuned on the ToC2ME dataset— we applied Micro-EQpolarity to the entire ToC2ME catalog, successfully inverting 2,519 high-quality focal mechanism

solutions (FMSs). This comprehensive dataset facilitated the identification of four distinct FMS types and enabled the analysis of events with magnitudes as low as -1.4. The resulting focal mechanisms revealed fine-scale fault structures, providing more detailed insights into the mechanisms of NS-Fault earthquake reactivation (Section 4.3.1) and the fluid diffusion process in NE-Fault (Section 4.3.2).

2 Data and Method

2.1 Data

The training data for the base model is sourced from the Southern California Seismic Network (SCSN) (Southern California Earthquake Data Center, 2013), consisting of 1,662,796 single-component waveforms recorded between 2000 and 2017. This dataset includes 831,398 waveforms for each of the upward and downward P-wave first-motion polarity classes. Each waveform has a duration of 6 seconds, capturing 3 seconds before and 3 seconds after the manually picked P-wave arrival time (Ross, Meier, & Hauksson, 2018). The dataset used for model fine-tuning is from the Tony Creek Dual Microseismic Experiment (ToC2ME) (Eaton et al., 2018). This experiment was conducted with a dense, shallow borehole geophone array (27 m depth) that recorded continuous three-component (3C) waveform data. A total of 69 three-component geophones were deployed in the boreholes, with an average station spacing of 500 m (Fig. 1). We manually picked 21,916 single-component waveforms from this dataset, using 90% of these waveforms (i.e., 19,724 single-component waveforms) for the actual fine-tuning process, and 10% of these waveforms (i.e., 2,192 single-component waveforms) for validation of our model during the training process. Moreover, we also manually prepared a testing set of 2,861 single-component waveforms sampled from the eastern, central, and western regions in the ToC2ME area to evaluate the performance of our proposed model.

The two datasets differ significantly in their magnitude ranges and characteristics. The training data from SCSN covers earthquakes with magnitudes ranging from approximately -0.8 to 7.2, with 90% of the data distributed between magnitudes 0.5 and 2.8. The dataset used for model fine-tuning from ToC2ME primarily contains events with magnitudes ranging from approximately -2.2 to 3.2, with 98.5% of events having magnitudes between -2.0 and 0.0, which is typical of microseismic event magnitude ranges.

2.2 Method

We develop a workflow for building a high-resolution focal mechanism catalog, specifically designed for microseismic events, and apply it to the entire earthquake waveform archive of the ToC2ME dataset. This workflow consists of two main steps (see Fig. 2). First, model is trained with microseismic data from ToC2ME to fine-tune the parameters of the pre-trained model, which outputs the Micro-EQpolarity model that determines P-wave polarities. In the second step, first-motion polarities determined in the model training stage are inverted for focal mechanisms, along with further quality control checks to ensure high-quality focal mechanism solutions. The details of each step are discussed in the following subsections.

2.2.1 Model Training

During the Model Training stage, the base deep learning (DL) model (see Fig. 3) employed in this study, named EQpolarity, is designed for polarity determination and has demonstrated superior performance in identifying P-wave first-motion polarities for small to moderate-sized earthquakes (Chen et al., 2024). EQpolarity consists of two main components: the convolutional block (Conv block) and the transformer block. The Conv block extracts feature maps from the input data, while the transformer block emphasizes the most relevant features by assigning high attention weights.

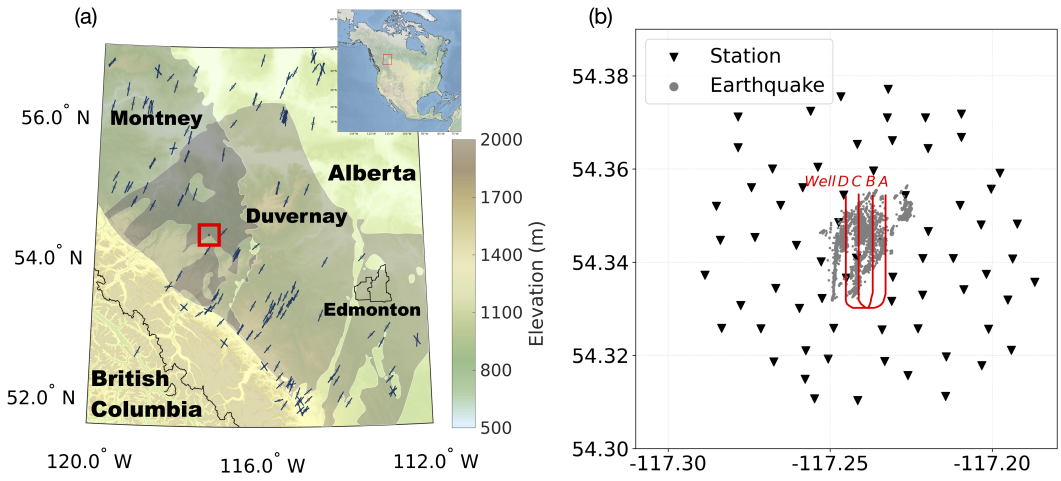

Figure 1. (a) Regional map of the ToC2ME study area (red box) in Alberta, situated between Montney and Duvernay. The inset map indicates the location of Alberta within North America. Blue segments indicate orientations of S_{Hmax} in Alberta from the World Stress Map. (b) Map of the ToC2ME monitoring configuration with 69 geophone stations (triangles) surrounding the hydraulic fracturing treatment wells (red lines), recording 21,619 events in ML -2.19 to 3.21. Gray dots represent the spatial distribution of 21,619 seismic events recorded from October 26 to November 30.

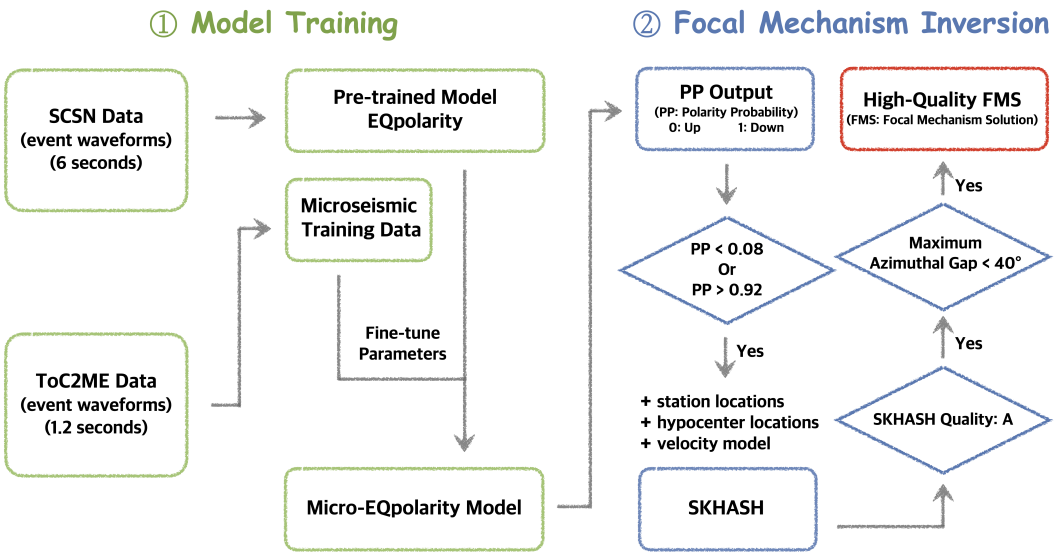

Figure 2. Workflow for calculating focal mechanisms of microseismic events using transfer learning to adapt the EQpolarity model for microseismic P-wave first-motion polarity determination. The workflow is divided into two main stages: Model Training and Focal Mechanism Inversion. The Model Training stage involves loading the pre-trained model trained on earthquake data from the SCSN, incorporating microseismic data, and fine-tuning parameters using ToC2ME microseismic data to produce the final Micro-EQpolarity model. In the Focal Mechanism Inversion stage, the SKHASH algorithm, combined with quality control checks, is used to derive high-quality focal mechanism solutions.

The Conv block comprises three layers: a 1D convolutional layer, an activation function, and a max-pooling layer. The mathematical operations for the Conv block are defined as follows:

$$F(i) = \sum_{m=0}^{M} G(i-m) * w(m),$$

$$\gamma(F) = \max(0, F),$$

$$O = \text{pool}(a) = \max(\gamma(a+q)),$$

where w is the kernel function with size M, γ represents the Rectified Linear Unit (ReLU) activation function, and q is the stride of the max-pooling layer. The Conv block uses a kernel size $M = 3$ and a pooling stride $q = 2$. By applying two consecutive Conv blocks, the output has a size of 150×200, with 200 feature maps.

The transformer block follows the Conv block and highlights the most significant features extracted. It consists of three normalization layers, a multi-head attention (MHA) layer, two stochastic depth dropout (SDD) layers, and a multilayer perceptron (MLP) (Hassani et al., 2021). The core component of the transformer is the MHA layer, which utilizes multiple self-attention (SSA) networks (Hassani et al., 2021; Vaswani, 2017). In this model, four SSA networks are employed, and their outputs are concatenated as follows:

$$\text{MHA}(Z) = [S_1(Z); \ldots; S_i(Z)],$$

where i is the number of SSA heads (ranging from 1 to 4) and Z is the input to the MHA layer. Each SSA network generates query (Q), key (K), and value (V) vectors through fully connected layers:

$$K = ZW_K, \quad Q = ZW_Q, \quad V = ZW_V,$$

where W_K, W_Q, and W_V are the weight matrices for the key, query, and value vectors, respectively. The SSA attention weight is computed using a softmax function:

$$H = \text{Softmax}\left(\frac{QK^T}{\sqrt{l}}\right),$$

where l represents the length of the query vector. The final output of the SSA is obtained through the dot product of the attention weight (H) and the value vector (V):

$$\text{SSA}(Z) = V \times H.$$

The normalization layers ensure that features have zero mean and unit variance (Ioffe, 2015). To enhance regularization, stochastic depth dropout (SDD) layers are employed, randomly dropping certain layers during training (Loshchilov & Hutter, 2016). The SDD rate is gradually increased across the four transformer blocks, ranging from 0 to 0.1 with a step size of 0.033 (Loshchilov & Hutter, 2016).

The final component is the MLP network, which processes the features output by the transformer block. The MLP comprises two fully connected layers, each followed by

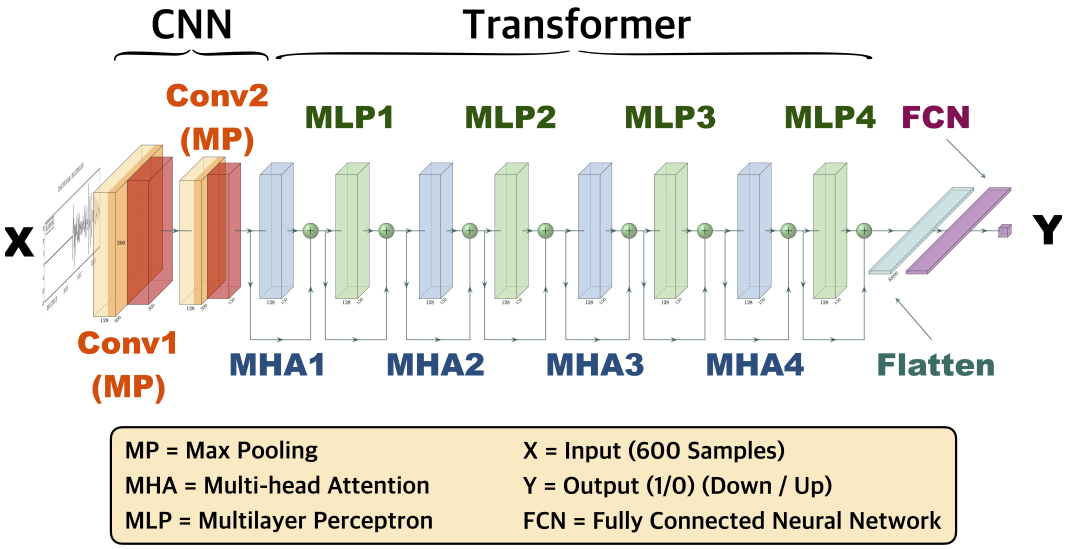

Figure 3. Architecture of the EQpolarity neural network for P-wave first-motion polarity determination. The model combines convolutional blocks and multi-head attention transformer blocks with 600-sample input. The data shape for each processing stage is noted at the bottom of the blocks.

a Gaussian Error Linear Unit (GELU) activation function (Hendrycks & Gimpel, 2016) and a dropout layer with a rate of 0.2. A final fully connected layer with a sigmoid activation function maps the extracted features to classify the polarities into up and down classes.

The EQpolarity model was pre-trained using the SCSN dataset, which contains 1,662,796 waveforms with their corresponding P-wave first-motion polarities in 6-second waveform segments. To enhance the model's performance in identifying microseismic events, we employed a transfer learning approach by fine-tuning the pre-trained model on the ToC2ME dataset (Eaton et al., 2018). A total of 21,916 single-component waveforms were manually selected and randomly divided into two subsets: a training subset comprising 19,724 waveforms (90%) for fine-tuning the proposed EQpolarity model, and a validation subset containing 2,192 waveforms (10%) for validating model performance throughout the training procedure. The data distribution between base and fine-tuning datasets for transfer learning can be seen in Table 1.

For the ToC2ME dataset, waveform data were filtered based on signal-to-noise ratio (SNR) to ensure retention of only high-quality waveforms that meet the standards for manual picking. Based on P-arrival time estimates, the waveforms were initially truncated to 10 seconds, with 5 seconds before and 5 seconds after the estimated P-wave arrival time. The P-wave signal window was defined as the 4.5–5.5 s time interval, while the noise window was set as the 0–4.5 s interval. The variances of the vertical component waveforms for both signal and noise were calculated as follows:

$$\mathrm{SNR} = \frac{\sqrt{\mathrm{var}_{Pz}}}{\sqrt{\mathrm{var}_{Nz}}}$$

where var_{Pz} denotes the variance of the P-wave signal, and var_{Nz} represents the variance of the noise. Waveform records with SNR values below 2 were discarded. Finally, the qualified waveforms were truncated to 1.2 seconds duration, encompassing 0.6 seconds before and after the first arrival time, ensuring that each waveform contained 600

Table 1. Data distribution between base and fine-tuning dataset for transfer learning

Region	Number of Waveforms
Southern California (SCSN)	1,662,796
Western Canada Sedimentary Basin (ToC2ME)	19,724

samples for model input. The pre-trained model was subsequently fine-tuned to develop the final Micro-EQpolarity model, which is optimized for microseismic polarity analysis.

2.2.2 Focal Mechanism Inversion

To determine the polarity of the corresponding waveforms, the screened waveforms were processed using the Micro-EQpolarity model to derive the probability distribution of first-motion polarities. Polarity records were retained only if their predicted probabilities exceeded 0.92 (classified as down) or were below 0.08 (classified as up), thereby filtering out low-confidence polarity data. Utilizing these high-confidence polarity records, the azimuth and take-off angles were computed based on refined earthquake locations and the associated velocity model (F. Zhang et al., 2022).

The focal mechanism solutions (FMSs) were then determined using SKHASH (Skoumal et al., 2024), which incorporates P-wave first-motion polarities while accounting for uncertainties in polarity observations and take-off angles to mitigate picking errors and derive the most reliable focal mechanism. To ensure the robustness of polarity projections during inversion, we retained only those focal mechanism solutions where the maximum azimuthal gap between adjacent stations was less than 40 degrees and whose quality rating from the SKHASH output was classified as A. Following this rigorous selection process, a total of 2,519 focal mechanism solutions were obtained, all of which met stringent high-quality control criteria.

3 Model Performance and Transfer Learning Effectiveness

In this section, we present a comprehensive evaluation of the Micro-EQpolarity model's performance and validate the effectiveness of the proposed transfer learning strategy. The evaluation consists of two main components: first, we assess the model's performance using the ToC2ME dataset through confusion matrix, classification accuracy, learning curves, and resolved magnitude distribution analyses; second, we analyze the effectiveness of the transfer learning scheme, examining how limited microseismic training data improves model performance.

3.1 Model Performance on ToC2ME Dataset

To evaluate the performance of the proposed model, we prepared a testing set from the ToC2ME dataset. This dataset consists of 2,861 single-component waveforms sampled from the eastern, central, and western regions in ToC2ME area. The testing and training sets are completely independent to ensure an unbiased evaluation.

The training process utilized 90% (i.e., 19,724 single-component waveforms) of the training set for model optimization, while the remaining 10% (i.e., 2,192 single-component waveforms) was used for validation. We employed the Adam optimizer (Kingma & Ba, 2017) to optimize the network parameters, with a learning rate set to 0.001. The Micro-EQpolarity model was trained for 50 epochs. The learning curves of the Micro-EQpolarity are presented in Fig. 4(a) and Fig. 4(b), respectively. After completing training, the Micro-

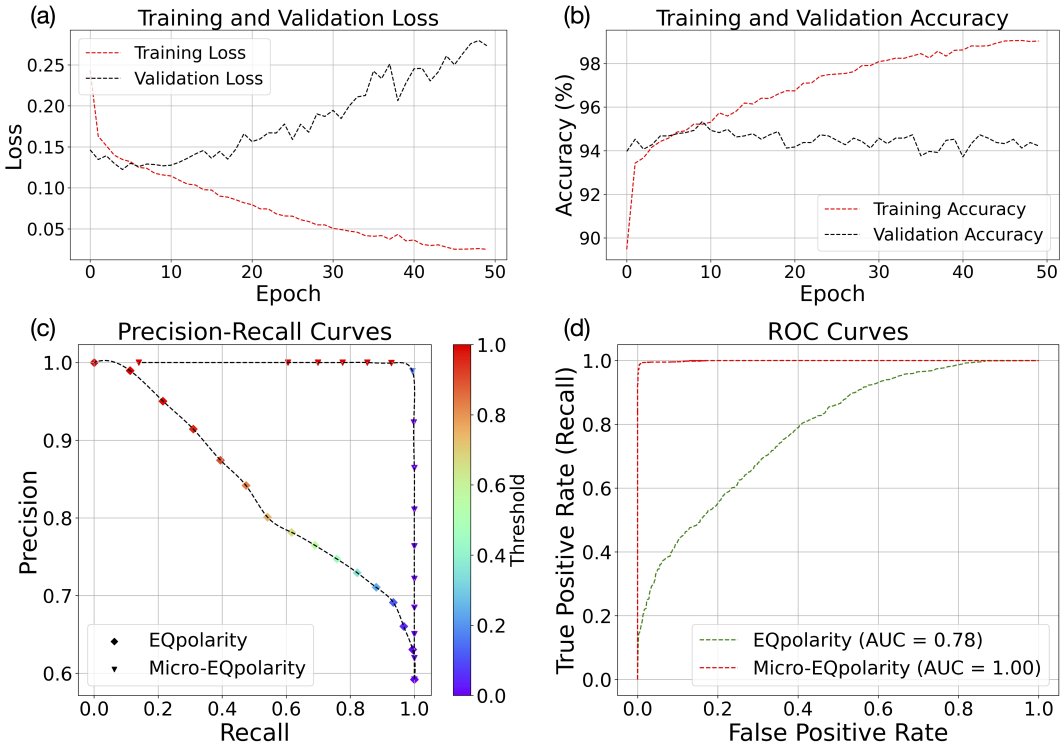

Figure 4. Learning curves of Micro-EQpolarity trained on ToC2ME data, showing (a) loss and (b) accuracy for both training and validation sets with a threshold of 0.5. Performance evaluation includes (c) precision-recall curves (d) ROC curves on ToC2ME test set.

Table 2. Confusion matrix of Micro-EQpolarity model on ToC2ME test set

	Up (True)	Down (True)
Up (Predicted)	1156 (99.06%)	12 (0.71%)
Down (Predicted)	11 (0.94%)	1682 (99.29%)

EQpolarity model was applied to predict the P-wave first-motion polarity on the testing set. To evaluate the model's classification performance, we present the confusion matrix in Table 2. A classification threshold of 0.5 was used, where probabilities exceeding the threshold were classified as class one, while probabilities below the threshold were classified as class zero.

To further assess the performance of the Micro-EQpolarity model, we compared its accuracy with the EQpolarity model pre-trained on the same base dataset but without utilizing transfer learning. The comparison results are summarized in Table 3, where the Micro-EQpolarity model achieves an accuracy of 99.20%. Fig. 4(c) illustrates the precision-recall (PR) curves for these two models on the ToC2ME testing set across different thresholds. Fig. 4(d) presents the receiver operating characteristic (ROC) curves for these models on the same testing set, where the area under the curve (AUC) for the ROC of Micro-EQpolarity is nearly 100%.

The Micro-EQpolarity model also demonstrates strong capability for the low-magnitude earthquake analysis. After applying the Micro-EQpolarity model to automatically determine focal mechanism solutions in the ToC2ME dataset containing 21,205 earthquake

Table 3. Accuracy of different models evaluated on the ToC2ME test set with varying fine-tuning datasets[a]

Model	Base Dataset	Fine-Tuning Dataset	Accuracy (%)
EQpolarity	SCSN	/	69.94
Micro-EQpolarity	SCSN	ToC2ME	99.20

[a]SCSN refers to data from Southern California, ToC2ME refers to the Tony Creek Dual Microseismic Experiment field program in Canada.

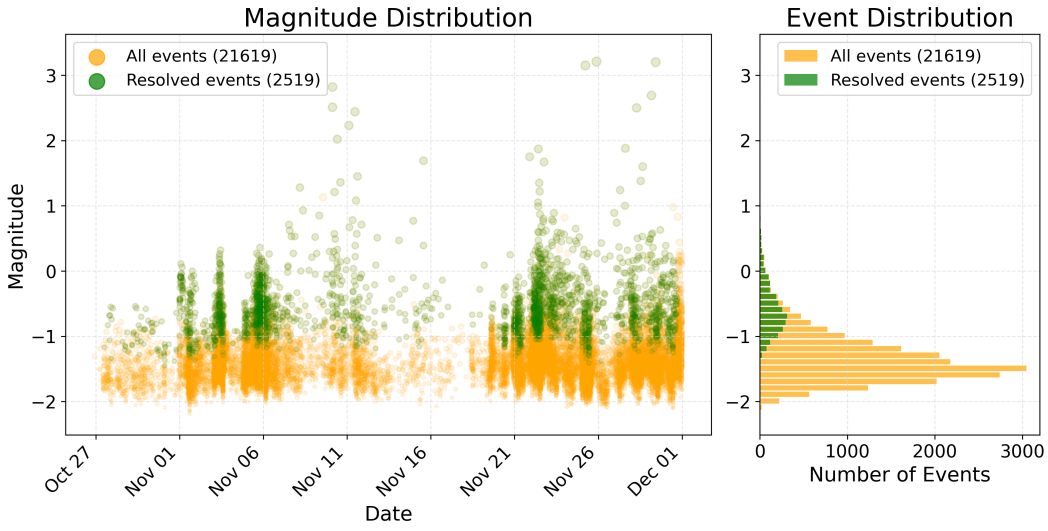

Figure 5. Magnitude distribution of seismic events in ToC2ME in late 2016, with the right panel showing a frequency histogram at 0.1 magnitude intervals. The analysis comprises 21,619 total seismic events (yellow dots) and 2,519 events with automatically resolved focal mechanisms (green dots). The resolved events extend to magnitudes as low as -1.4, as illustrated in both the temporal evolution (left) and frequency distribution (right).

events, we successfully obtained 2,519 high-quality focal mechanism solutions that all satisfied strict quality control criteria (for details, see Section 2.2). It shows high accuracy, with P-wave first-motion polarity predictions showing good agreement with observed waveforms and providing tight constraints on nodal plane locations, as exemplified by a magnitude -1.07 event in Fig. S1. Remarkably, leveraging the dense array configuration and the highly efficient workflow of our Micro-EQpolarity model, we achieved successful focal mechanism inversion for events with magnitudes as low as -1.4 throughout the entire monitoring period (Fig. 5).

3.2 Effectiveness of transfer learning scheme

To evaluate the effect of training ratio on the fine-tuning dataset when applying transfer learning, we fine-tune the proposed model six times independently, with each case using a different training ratio. Specifically, we use training ratios of 1%, 10%, 30%, 50%, 70%, and 90% from the manually picked ToC2ME training dataset (21,916 single-component waveforms) for the six cases, respectively. For all six cases, the testing set remains the same, consisting of 2,861 single-component waveforms sampled from the eastern, central, and western regions of the ToC2ME area.

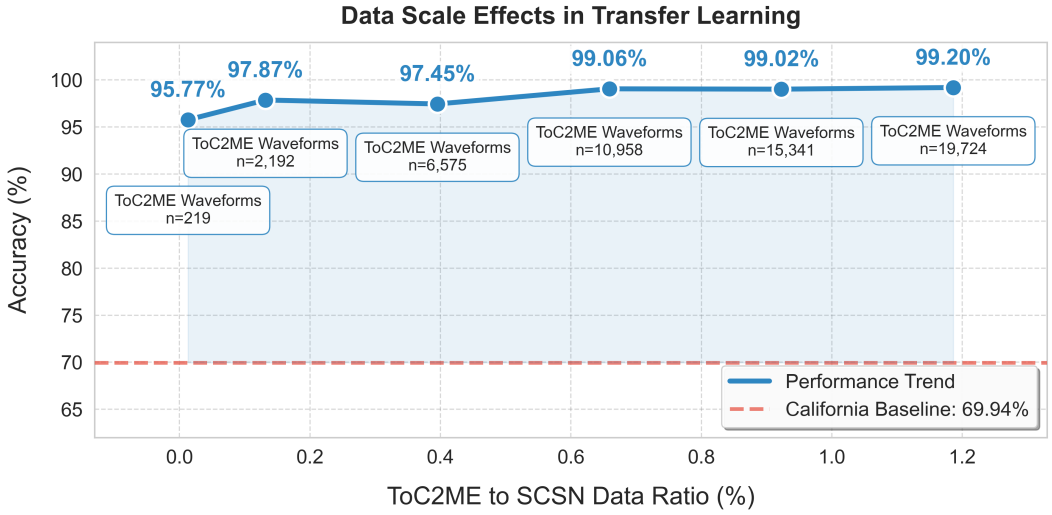

Figure 6. Model performance trends with varying transfer learning data sizes. Starting with a baseline California accuracy of 69.94%, the model's performance improves as the data ratio increases, reaching from 95.77% (n=219) to 99.20% (n=19,724) at its peak - a total improvement of 29.26 percentage.

Fig. 6 shows the test accuracy using different training ratios for transfer learning. The test accuracy generally improves as the training ratio increases due to enhanced learning capability of the model when using a larger dataset for fine-tuning (Chen et al., 2024), ranging from 95.77% (n=219) to 99.20% (n=19,724). Compared to the baseline California accuracy (i.e., pre-trained EQpolarity model's accuracy) of 69.94%, a total improvement of 29.26 percentage points is achieved. Remarkably, by fine-tuning the model with only 219 ToC2ME waveforms (0.013% of the SCSN base dataset) and their associated polarity records, the model achieves a high accuracy of 95.77% on the microseismic testing set. This demonstrates that through the transfer learning scheme, Micro-EQpolarity can achieve an optimal balance between polarity classification accuracy and training set preparation efficiency.

4 Comprehensive Focal Mechanism Catalog and Its Applications to Fault System Analyses

In preceding sections, we proposed our Micro-EQpolarity model for microseismic P-wave first-motion polarity determination and developed a workflow for focal mechanism inversion based on our proposed model with strict quality control. Here, by utilizing this workflow, we obtained a comprehensive focal mechanism catalog in the ToC2ME region with rigorous quality control, demonstrating strong consistency and significant improvements in quantity compared to previous work. To better understand the induced seismicity in ToC2ME, we apply this catalog to investigate fault reactivation mechanisms and fluid diffusion processes in different fault systems.

4.1 Comprehensive Catalog of Focal Mechanism Solutions in Western Canada

Using the fine-tuned Micro-EQpolarity model and the workflow (Fig. 2) built upon this model, we obtained 2,519 focal mechanism solutions from 21,205 earthquake events in the ToC2ME dataset, all meeting rigorous quality control standards (for details, see

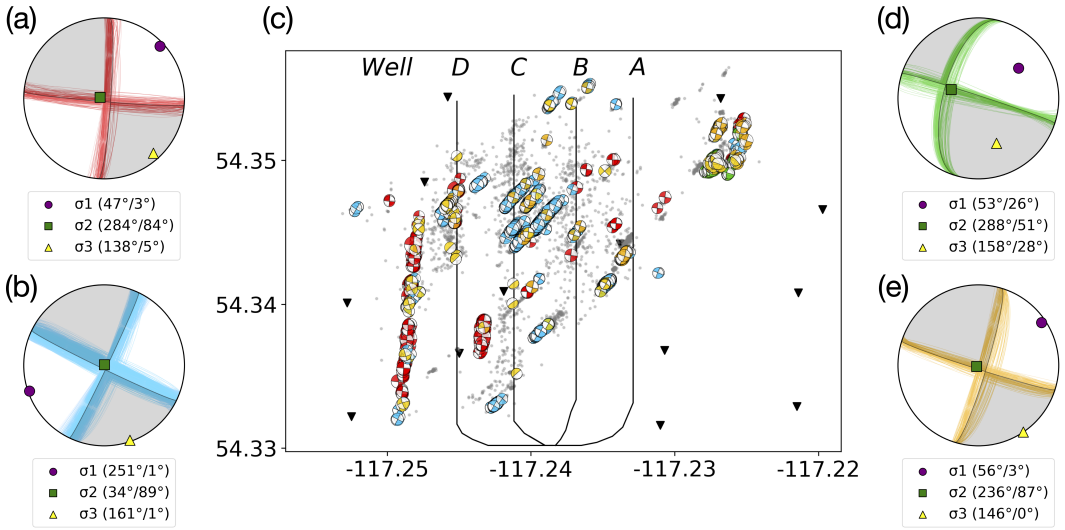

Figure 7. Classification and map view of focal mechanism solutions in ToC2ME. (a) Group 1: north-south trending, high-angle strike-slip faults; (b) Group 2: northeast-southwest trending, high-angle strike-slip faults; (c) Map view of high-quality focal mechanism solutions in ToC2ME. Gray dots represent the distribution of 21,619 seismic events, with geophone stations (triangles) positioned around hydraulic fracturing wells (black lines). The colors of the focal mechanisms correspond to their respective groups, and the size of each focal mechanism reflects its magnitude; (d) Group 3: northeast-southwest trending, moderately dipping strike-slip faults; (e) Group 4: high-angle strike-slip faults with strike orientations intermediate between Groups 1 and 2. Purple circles, green squares, and yellow triangles denote the orientations of maximum principal stress (σ_1), intermediate principal stress (σ_2), and minimum principal stress (σ_3), respectively.

Section 2.2). The spatial distribution of these high-quality focal mechanisms is shown in Fig. 7(c). Based on the strike and dip angles of these high-quality focal mechanism solutions, the 2,519 events were categorized into five groups (Fig. 7). Group 1 , consisting of 462 events, is primarily located to the west of the hydraulic fracturing wells, with nodal plane orientations (mean value ± standard deviation) of 4.15° ± 3.88°, closely aligning with the north-south fault orientation (Fig. 7(a)). Group 2 includes 1,648 events, which are mainly situated in the middle of the hydraulic fracturing wells, with nodal plane orientations averaging 25.48° ± 3.04° (Fig. 7(b)). Group 3 comprises 130 events, located primarily to the northeast of the hydraulic fracturing wells, with nodal plane orientations averaging 15.35° ± 2.19° (Fig. 7(d)). Group 4 contains 205 events, with nodal plane orientations averaging 16.84° ± 2.03° (Fig. 7(e)). The remaining 74 events, categorized as "Other," exhibit focal mechanisms that differ from those of the other four groups. Events in Groups 1, 2, and 4 predominantly show strike-slip focal mechanisms with sub-vertical planes, with inverted dip angles of 82.4° ± 10.72°, 86.57° ± 5.50°, and 80.54° ± 11.81° for Groups 1, 2, and 4, respectively. In contrast, events in Group 3 exhibit slip along a more shallow-dipping plane, with an inverted dip angle of 50.71° ± 5.11°.

Moreover, we conducted stress inversion for each group (Groups 1–4) using the respective average focal mechanisms, utilizing the stress inversion package described in (Busetti et al., 2014; Reches et al., 1992). Previous studies (Shen et al., 2019) reported that the average direction of the maximum horizontal compression (SH_{max}) in Fox Creek, Alberta, is approximately N43°E. This finding aligns well with the general trend of the maximum principal stress directions obtained for each group shown in Fig. 7.

4.2 Comparative Analysis of the Existing Catalog

To assess the reliability of our catalog, we extract 160 common events and compare focal mechanism consistency between our catalog and that of Yang et al. (2024) (167 solutions). We employ the Kagan angle (Kagan, 1991), defined as the smallest angle needed to rotate the principal axes of one moment tensor to align with those of another (Tape & Tape, 2012), to quantify the similarity between corresponding events in both catalogs. The deviations for matched events range from 1.56° to 29.37°, with an average Kagan angle of 10.07°. Among all 160 common focal mechanisms, 97.5% exhibit Kagan angles less than 25° (the uncertainty threshold for quality A focal mechanisms in SKHASH (Skoumal et al., 2024)), while all angles remain below 35° (the threshold for quality B focal mechanisms (Skoumal et al., 2024)). These results demonstrate excellent consistency with the Yang et al. (2024) catalog, with differences generally within acceptable uncertainty ranges.

Our catalog also shows significant quantitative improvements in magnitude, temporal, and spatial distributions. In terms of magnitude distribution, our catalog contains more lower-magnitude events. As shown in Fig. 8(a), the peak magnitude (ML) in the existing catalog is centered around 0, whereas our catalog peaks at approximately -1.0. Moreover, the maximum event count in the existing catalog is approximately 60, whereas our catalog reaches nearly 570. Regarding temporal distribution, our catalog records more seismic events per day compared to the existing catalog, as shown in Fig. 8(b). In addition, a significant gap in seismicity can be observed around November 17, which coincides with two hydraulic fracturing stages (F. Zhang et al., 2022). For spatial distribution, as shown in Fig. 8(c), our catalog includes a greater number of focal mechanism solutions in most regions, enabling the discovery of more detailed fault structures.

4.3 Fine-scale fault structures revealed by focal mechanisms

The high-resolution earthquake catalog (F. Zhang et al., 2022) and the improved fault mechanism solutions (FMSs) offer enhanced capabilities for detailed characterization of fault zone structures. This study focuses on two clusters: NS-Fault in the western part of the study area, and NE-Fault in the eastern part, as shown in Fig. 9.

4.3.1 Fault Reactivation Mechanisms in the NS-Fault

The extensive FMSs provide new constraints on fault zone properties and their reactivation mechanisms. The FMSs on the NS-Fault can be classified into two major groups: N-S trending and NE-SW trending high-angle strike-slip faults. The N-S trending faults, which correspond to the group 1 faults shown in Fig. 7(a) and the red circles in Fig. 10, exhibit consistent slip behaviors in conjunction with injection, with approximately 180° orientation. In contrast, the NE-SW trending faults, which correspond to the group 2 faults shown in Fig. 7(b) and the blue circles in Fig. 10, show systematic differences in strike direction from the N-S trending faults and are only activated in the second stage, following the occurrence of large earthquakes in group 1.

To examine the complex triggering mechanism of earthquakes on this N-S fault, we conduct a Mohr-Coulomb failure analysis using our high-quality focal mechanisms. This requires an accurate constraint on the principle stress tensor. Therefore, we first invert for the background stress regime (SH_{max} azimuth = N53.1°E) using 290 high quality FMSs (Skoumal et al., in review). Next, to determine the principal stresses at focal depth (about 3.2 km), we utilize the 3D predictive model developed by Shen et al. (Shen et al., 2019), which provides stress state distribution over a 150 km × 150 km area centered near Fox Creek and encompasses our study area. From this model and available borehole measurements at focal depth in the study area (centered at 117.2485°W, 54.3400°N), we obtain an intermediate principal stress σ_2 of 80.480 MPa and a pore pressure of 55.99 MPa. The minimum principal stress σ_3 is determined to be 65.99 MPa, referring to the

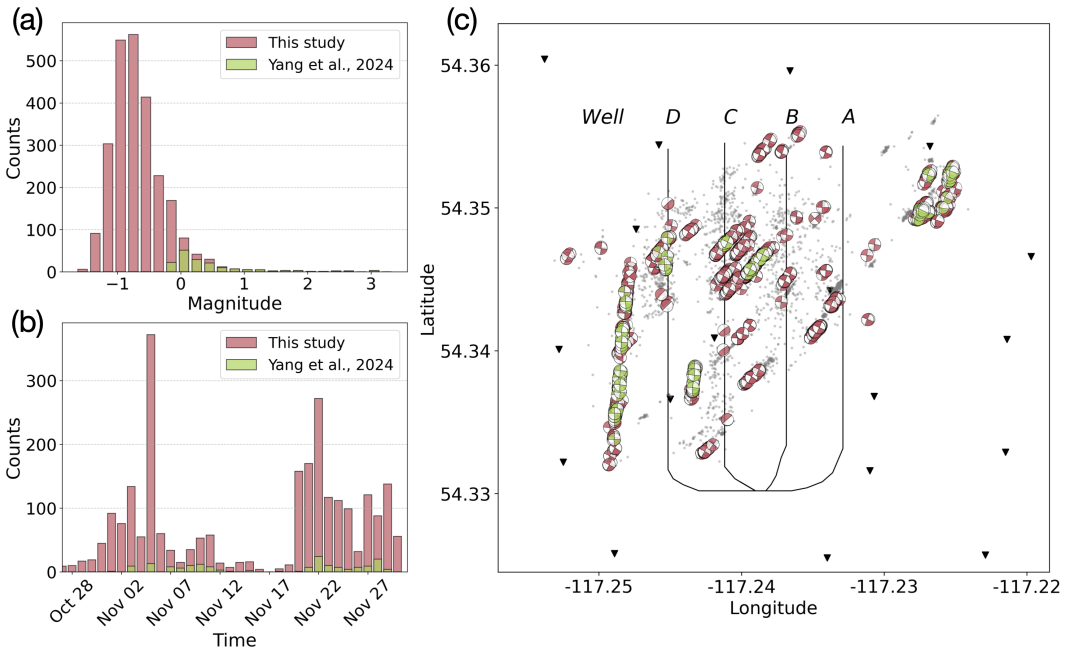

Figure 8. Comparison of focal mechanism solutions between this study and the existing catalog (Yang & Wang, 2024) in ToC2ME. (a) Histogram of event magnitudes for the focal mechanism solutions in this study's catalog (red) and the existing catalog (green). (b) Histogram of event occurrences over time, showing the temporal distribution of focal mechanism solutions in both catalogs. (c) Spatial distribution of focal mechanisms, comparing this study's catalog (red) with the existing catalog (green). Black triangles indicate station locations, and labeled vertical lines (A–D) denote wells.

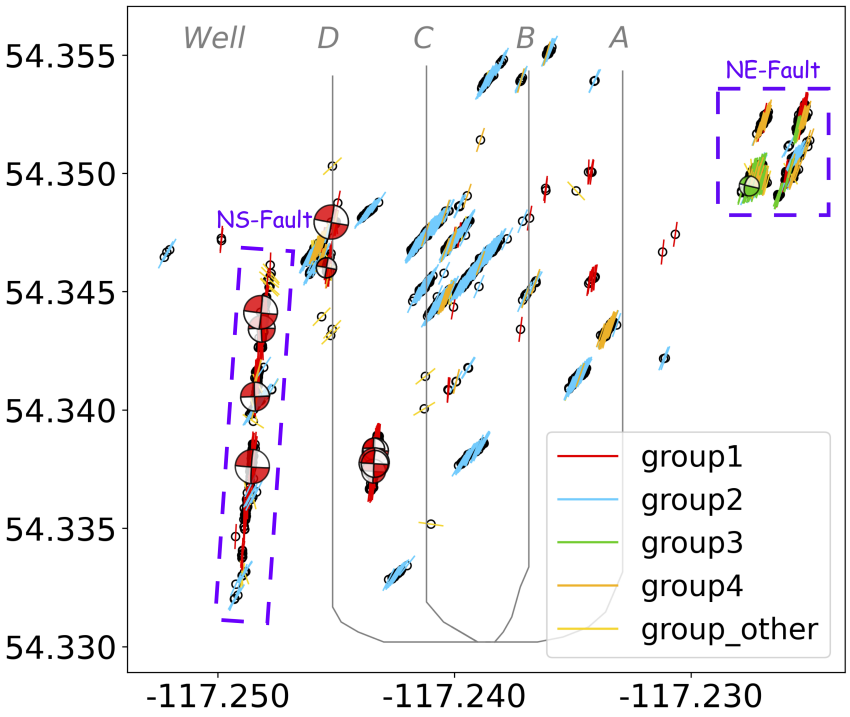

Figure 9. Spatial distribution of focal mechanism solutions across the study area. Line segments represent fault strikes, colored by Groups 1–4 (as defined in Fig. 7). Two clusters, NS-Fault and NE-Fault, are highlighted within the purple dashed frames. Beachballs are plotted for the larger-magnitude events, specifically those with magnitudes greater than 1.86.

approximate minimum principal effective normal stress value from Zhang et al. (H. Zhang et al., 2019). Finally, considering the critical stress state and hydrostatic pressure conditions of the seismogenic fault (Terakawa et al., 2012), under which the Mohr circle becomes tangent to the Coulomb failure envelope, we determine σ_1 to be 86.650 MPa.

These well-constrained stress parameters enable us to evaluate the failure susceptibility of different fault groups (Fig. 11). The analysis indicates that NE-SW trending faults (Group 2) are theoretically most prone to failure. This is because the average strike of Group 2 forms approximately a 28° angle with the SH_{max} azimuth (see Section 4.1). According to the Mohr-Coulomb criterion, the optimal failure angle is 45° - $0.5\tan^{-1}\mu$. Using Byerlee's empirical friction coefficient $\mu \approx 0.6$, this yields an optimal angle of ~30°, closely matching the differential angle between the strike direction of this fault group and the SH_{max} azimuth (C. Zhang et al., 2024; Byerlee, 1967). However, Group 2 faults began to reactivate around November 29, considerably later than other fault groups (Fig. 10), which does not correspond to their expected higher failure susceptibility. The possible explanations are as follows: Master faults usually have higher cumulative slip than subsidiary fault zones in strike-slip fault systems (Cembrano et al., 2005). The higher cumulative slip typically results in thicker and more continuous gouge layers (Scholz, 1987), which means more gouge material is present in master faults, causing cohesion degradation (Giorgetti et al., 2015). Therefore, Group 2 faults (the subsidiary faults) exhibit greater cohesion (C) values (Fig. 12(c)). On the other hand, large-displacement faults become progressively polished over time (Sagy et al., 2007), which causes Group 1 faults (the master faults) to have lower friction coefficients compared to Group 2 faults (Fig. 12(b)). Thus, despite Group 2 faults having higher stress states that theoretically make them

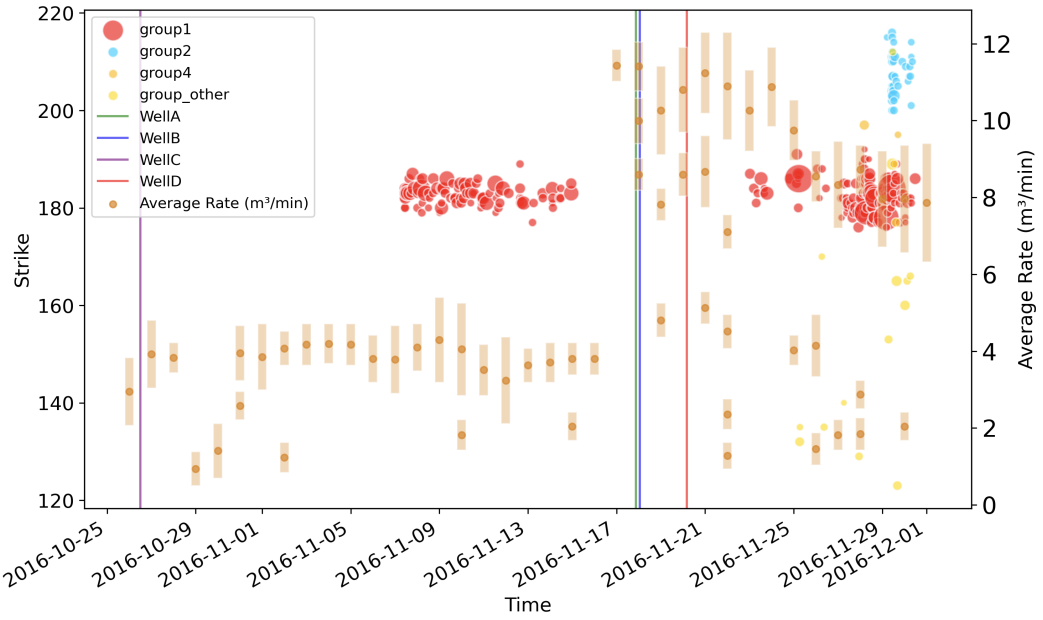

Figure 10. Correlation within the NS-Fault fault among hydraulic fracturing times for each well, focal mechanism strikes (normalized to 90°–270°) in the NS-Fault fault, and injection rates. Circles represent the focal mechanism strikes, with sizes proportional to earthquake magnitudes and colored according to Groups 1–4 (as defined in Fig. 7). Vertical lines indicate the start times of hydraulic fracturing for each well (green: Well A, blue: Well B, purple: Well C, red: Well D). Orange points represent the average injection rate, derived from publicly available daily injection rate data (Eaton et al., 2018).

more susceptible to failure, their higher cohesion and friction coefficients result in delayed reactivation compared to the master faults.

The additional Coulomb failure stress (ΔCFS) required to trigger Group 2 fault reactivation may primarily originate from Coulomb static stress transfer and elevated pore fluid pressure (Fig. 12(a)). One possible mechanism may as follows: Around November 17, increased injection rates (Fig. 10) transported additional fluids through preexisting fracture corridors, elevating fluid pressure and triggering larger earthquakes (Igonin et al., 2021). Simultaneously, residual fluids from the first hydraulic fracturing stage (October 26 to November 16, 2016) lubricated the faults, pushing the system toward a critical state. An earthquake with magnitude $M_L > 3$ and distinct fault topology (B. Q. Li, 2025) subsequently occurred, inducing Coulomb static stress transfer that created favorable conditions for activating secondary faults approaching critical stress states. Notably, all secondary faults (Group 2 and Group "Other") are located in regions of positive ΔCFS (B. Q. Li, 2025), supporting their increased likelihood of reactivation. However, solid evidence for the fluid conduits presented here remains limited. Moreover, the NS-Fault cluster is predominantly characterized by a fault system comprising two distinct groups. Group 1 faults trend north-south and constitute the primary fault zones with an average strike of 4.15°, acting as major structural features. Group 2 faults trend northeast-southwest with an average strike of 25.48° and function as secondary splay faults that intersect the primary structures at oblique angles, forming characteristic en-echelon patterns. Significant variations in focal mechanism strikes are observed along the major fault zones of the NS-Fault cluster (Fig. 9), likely corresponding to Riedel shears within bounded shear conduits (Weir et al., 2022).

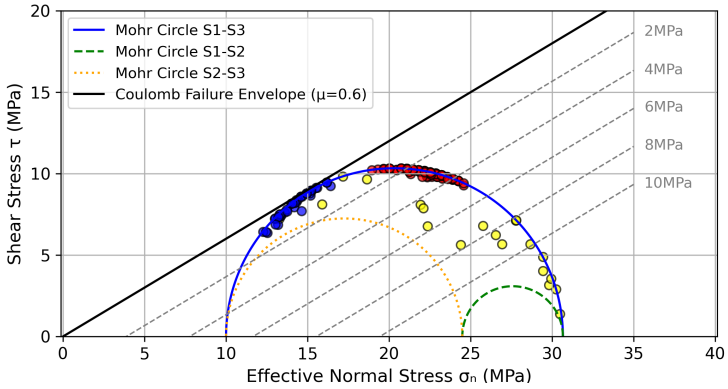

Figure 11. Mohr-Coulomb failure stress analysis on NS-Fault area. Mohr circle diagram showing stress conditions in the study area. Blue circles represent the stress state of Group 2 faults trending northeast-southwest, red circles represent the stress state of Group 1 faults trending north-south, and yellow circles represent the stress state of Group "Other" fault groups, according to (Fig. 7). Dashed lines indicate reference lines for the Coulomb failure stress (ΔCFS) required for failure.

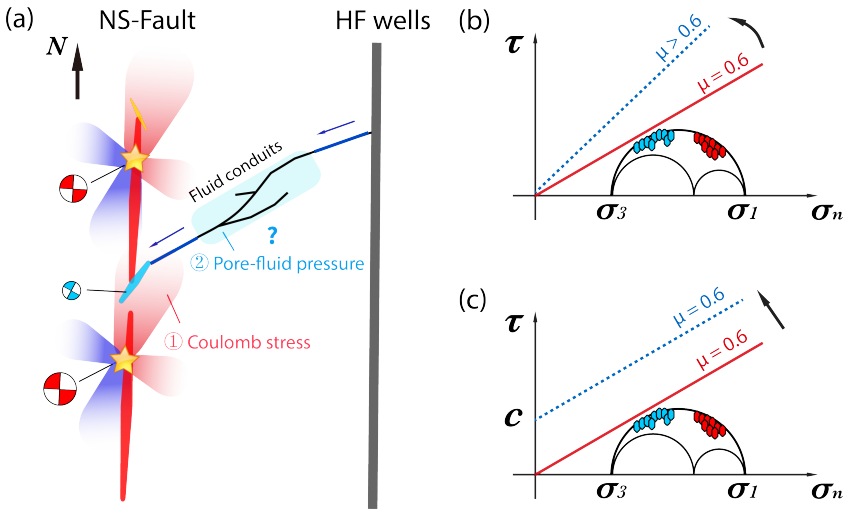

Figure 12. Schematic representation of fault reactivation mechanisms in the NS-Fault area. (a) shows the fault structure schematic of the western major fault and its triggering process (the combined effect of pore fluid pressure and Coulomb static stress), which causes the reactivation of Group 2 faults. The red represents Group 1 north-south striking strike-slip faults, while the yellow and blue faults represent Group 2 faults trending northeast-southwest and Group "Other" fault groups, respectively. The stars represent main earthquakes ($M > 3$), and the blue and red shadows show the influence range of Coulomb static stress (the red part indicates positive ΔCFS, and the blue part shows negative ΔCFS (B. Q. Li, 2025)). On the right side of Figure (a), the pore-fluid pressure is shown, whose increase during injection phases causes the reactivation of these faults. Question mark represents that the fluid conduits here are still uncertain.; (b) represents the Mohr-Coulomb failure stress analysis where the friction coefficient (μ) of the Group 2(blue) is higher; (c) shows the case where the cohesion (C) of the Group 2(blue) faults is greater.

4.3.2 Fluid Diffusion Process in NE-Fault

In the northeastern part of the study area (NE-Fault), to gain a more comprehensive understanding of fault activation, we relaxed the constraints on the focal mechanism solutions, requiring that the maximum azimuthal gap between adjacent stations be less than 40 degrees and that the quality rating from the SKHASH output be classified as A or B. As a result, we identified 913 focal mechanism solutions within NE-Fault, along with 156 low-dip faults.

Low-dip faults are characterized by increased down-dip extent and reduced normal stress, resulting in higher integrated fluid flux values relative to steep faults (Ford et al., 2009). Therefore, we initially regard low-dip faults as the primary conduits for fluid diffusion. Fluid pore pressure transfer plays a crucial role in fault activation, and these faults likely serve as preferential pathways due to their broader permeable zones resulting from increased fault-fluid contact areas. To test this hypothesis, we analyze the spatiotemporal distribution of low-dip faults in relation to the characteristic diffusion distance in a two-dimensional diffusion process (Fig. 13), which is given by:

$$D = \sqrt{4\pi dt} \tag{1}$$

where D represents the fluid diffusion front, with the location of the earliest recorded seismic event serving as the initial reference point. The parameter d denotes the diffusion coefficient (m^2/s), and t represents the time elapsed since the earliest recorded seismic event. We compare potentially reasonable diffusion coefficients within the range of 0.01 to $0.1\,m^2/s$. The best-fit diffusion coefficient is determined to be $0.0316\,m^2/s$, which encompasses almost all the low-dip fault locations.

Furthermore, given that fluid pressure along with fluid diffusion is considered a primary mechanism for fault activation (Igonin et al., 2021), we present the fluid diffusion sequences for six distinct faults in NE-Fault, highlighting key moments of their activation, as shown in Fig. 14. The main activation process began on November 20, when fluid first reached the southwestern part of Fault 1. This initial fluid arrival subsequently triggered the activation of Faults 2, 3, 4, 5, and 6 as the diffusion progressed (Fig. 15). Notably, Fault 3 appears to act as a "transfer station," facilitating fluid diffusion both eastward (toward Faults 4 and 5) and westward (toward Fault 6). This behavior may be attributed to the complex structure of its low-dip fault system (Fig. 15). Consequently, the activation of Faults 1, 2, 4, and 5 likely propagated from southwest to northeast, while Fault 6 exhibited an opposite activation direction, from northeast to southwest (Fig. 15). Moreover, a dense cluster of seismic events occurred in a short period north of Fault 1. This localized seismic activity may have resulted from poroelastic stress transfer, further contributing to fault instability.

Based on these observations, we propose the following fluid diffusion process in NE-Fault: During the first stage of hydraulic fracturing (i.e., 26 October to 16 November 2016), well C injected fluid (Fig. 10), causing the fluid to migrate along a southwest-to-northeast trending fracture network. The fluid reached the large NS-Fault fault to the west (Section 4.3.1), but its eastward influence remained limited. Meanwhile, the fluid continued migrating eastward, eventually reaching the NE-Fault fault system. This process weakened the fault strength, although it might not immediately trigger activation. During the second stage of hydraulic fracturing (17 November to 30 November), increased fluid pore pressure resulting from additional fluid injection and poroelastic stress transfer further destabilized the pre-weakened faults, rendering them highly susceptible to activation. (Fig. 15).

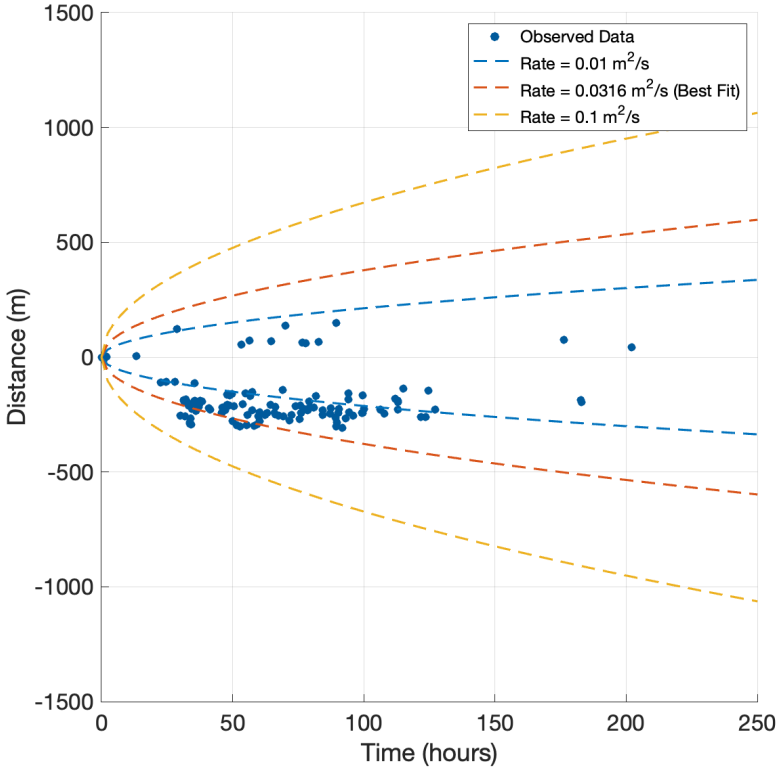

Figure 13. Spatiotemporal fluid diffusion fit for low-dip faults in NE-Fault. The dark blue dots represent the triggering times and spatial distribution of low-dip faults in NE-Fault, with the initial time and location corresponding to the earliest recorded seismic event. The blue dashed line represents a fluid diffusion rate of 0.01 m^2/s, the red dashed line represents a fluid diffusion rate of 0.0316 m^2/s (the best fit for fault triggering), and the yellow dashed line represents a fluid diffusion rate of 0.1 m^2/s.

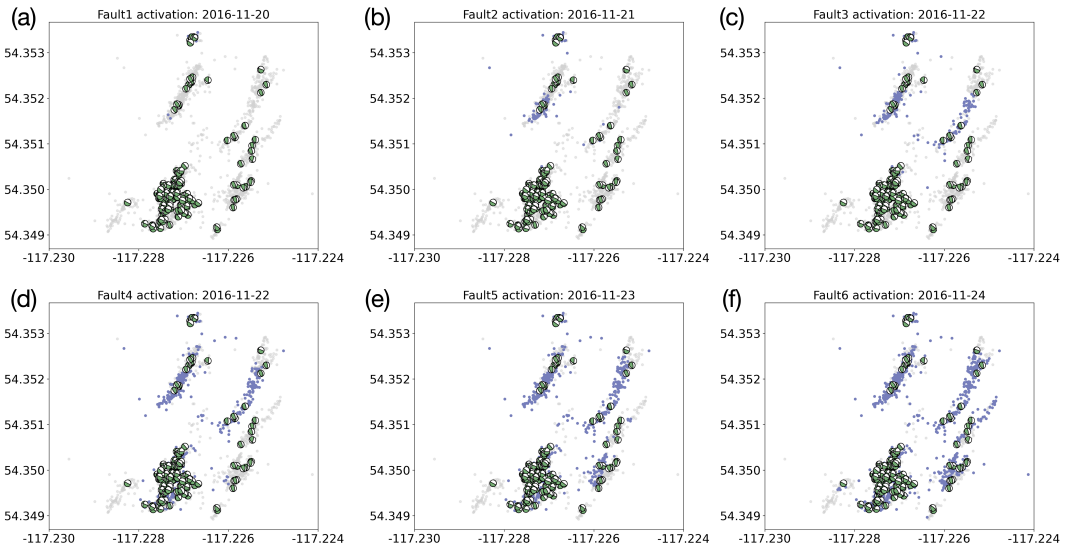

Figure 14. Sequential earthquake activation process in NE-Fault. Panels (a)–(f) illustrate the key moments marking the initiation of fault activation for Faults 1–6 as time progresses. Blue dots represent earthquakes that have been triggered, while gray dots indicate those that have not yet been activated. Low-dip faults are depicted, acting as fluid diffusion conduits that facilitate the activation process.

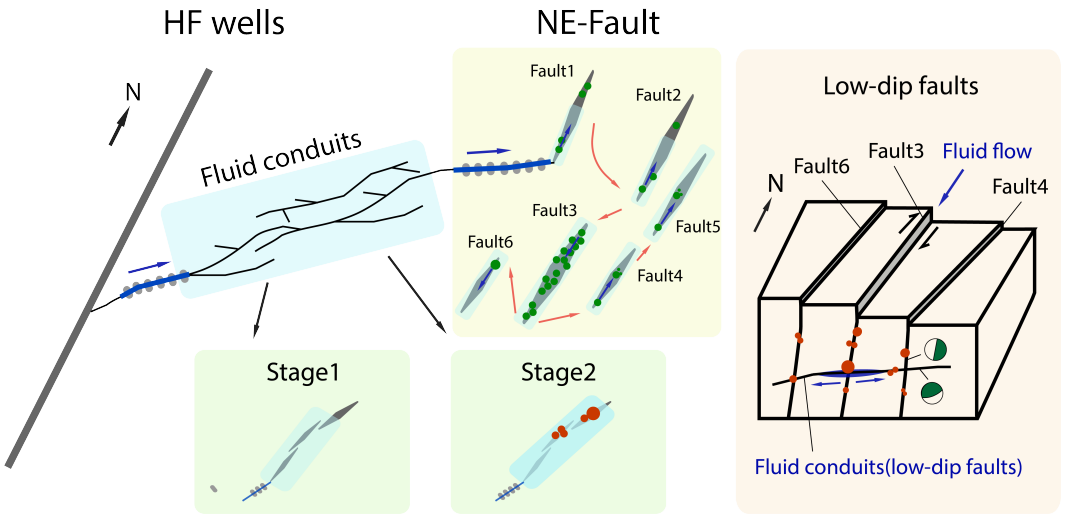

Figure 15. Schematic representation of the fluid diffusion process in NE-Fault. Fluid initially travels through the fluid conduits to the NE-Fault. "Stage 1" illustrates the process of fault strength weakening, while "Stage 2" depicts the destabilization of these weakened faults due to increased fluid pore pressure or poroelastic stress transfer. The circles (both red and green) represent earthquakes, with the circle size corresponding to the magnitude. Blue arrows indicate the direction of fluid diffusion within each fault, while red arrows represent the fluid diffusion direction between faults 1-6. On the right side, low-dip faults are shown, acting as fluid conduits in NE-Fault, with faults 3, 4, and 6 as examples. Based on extensive FMS data, low-dip faults are located beneath or within faults 3, 4, and 6, where high-dip angle faults also occur. The corresponding beachball plots are shown in the side view.

5 Conclusion

In this study, we developed a more comprehensive catalog of focal mechanism solutions in Western Canada using the Micro-EQpolarity model. This machine learning-based model, designed for determining microseismic P-wave first-motion polarity, leverages a transfer learning approach. The Micro-EQpolarity model achieved exceptional accuracy (>99%) on microseismic datasets, which are often characterized by low signal-to-noise ratios and smaller magnitudes. Based on this model, we developed an efficient workflow for automatically solving focal mechanisms. This led to the successful inversion of 2,519 high-quality focal mechanism solutions, producing a catalog more than four times larger than those from previous studies. These massive, high-fidelity focal mechanisms enabled the identification of four distinct focal mechanism types and extended the analysis to events with magnitudes as low as -1.4.

Furthermore, the resulting extensive and high-quality focal mechanisms reveal the detailed structure of re-activated faults in Western Canada, providing insights into the mechanisms of NS-Fault earthquake triggering and the fluid diffusion process in NE-Fault. In the NS-Fault cluster, our analysis reveals two possible reactivation mechanisms based on Mohr-Coulomb failure analysis. Despite Group 2 faults (trending northeast-southwest at ∼25.48°) being theoretically most susceptible to failure due to their optimal ∼28° angle with SH_{max} (N53.1°E), they exhibited delayed reactivation until November 29. This suggests: (1) higher friction coefficients due to structural immaturity of fault intersections lacking well-developed gouge layers and exhibiting rougher surfaces, and (2) enhanced cohesion from complex fracture networks with tightly interlocked angular clasts providing geometric resistance. Fault reactivation was driven by combined effects of Coulomb static stress transfer from a $M_L > 3$ earthquake and elevated pore-fluid pressure from increased injection rates around November 17, with all secondary faults located in regions of positive ΔCFS. As for the NE-Fault cluster, the two-stage hydraulic fracturing continuously facilitated the propagation of fluid into the NE-Fault cluster. Initially, fluid reached the southwestern part of Fault 1 and then propagated to Faults 2, 3, 4, 5, and 6 (Fig. 15), where Fault 3 appears to function as a "transfer station," facilitating fluid diffusion both eastward and westward, with low-dip faults acting as fluid conduits.

6 Data and Resources

The waveforms, trimmed to 5 seconds before and 5 seconds after the P-wave arrival time in the ToC2ME dataset, are available at `https://zenodo.org/records/14185578`. The online repository for the Micro-EQpolarity project can be found on GitHub: `https://github.com/chenyk1990/jiachenToc2Me`.

Acknowledgments

The research is supported by the funds Zhejiang University Chu Kochen Honors College In-Depth Scientific Research Training Project Funding.

References

Busetti, S., Jiao, W., & Reches, Z. (2014). Geomechanics of hydraulic fracturing microseismicity: Part 1. shear, hybrid, and tensile events. *American Association of Petroleum Geologists Bulletin*, *98*, 2439–2457. doi: 10.1306/05141413123

Byerlee, J. D. (1967). Frictional characteristics of granite under high confining pressure. *Journal of Geophysical Research (1896-1977)*, *72*(14), 3639-3648. Retrieved from `https://agupubs.onlinelibrary.wiley.com/doi/abs/10.1029/JZ072i014p03639` doi: https://doi.org/10.1029/JZ072i014p03639

Cembrano, J., González, G., Arancibia, G., Ahumada, I., Olivares, V., & Herrera, V. (2005). Fault zone development and strain partitioning in an extensional

strike-slip duplex: A case study from the mesozoic atacama fault system, northern chile. *Tectonophysics*, *400*(1), 105-125. Retrieved from https://www.sciencedirect.com/science/article/pii/S0040195105000843 doi: https://doi.org/10.1016/j.tecto.2005.02.012

Chai, C., Maceira, M., Santos-Villalobos, H. J., Venkatakrishnan, S. V., Schoenball, M., Zhu, W., ... Team, E. C. (2020). Using a deep neural network and transfer learning to bridge scales for seismic phase picking. *Geophysical Research Letters*, *47*(16), e2020GL088651. Retrieved from https://agupubs.onlinelibrary.wiley.com/doi/abs/10.1029/2020GL088651 (e2020GL088651 2020GL088651) doi: https://doi.org/10.1029/2020GL088651

Chen, Y., Saad, O. M., Savvaidis, A., Zhang, F., Chen, Y., Huang, D., ... Aziz Zanjani, F. (2024). Deep learning for p-wave first-motion polarity determination and its application in focal mechanism inversion. *IEEE Transactions on Geoscience and Remote Sensing*, *62*, 1-11. doi: 10.1109/TGRS.2024.3407060

Cheng, Y., Hauksson, E., & Ben-Zion, Y. (2023). Refined earthquake focal mechanism catalog for southern california derived with deep learning algorithms. *Journal of Geophysical Research: Solid Earth*, *128*, e2022JB025975. Retrieved from https://doi.org/10.1029/2022JB025975 doi: 10.1029/2022JB025975

Deichmann, N., & Ernst, J. (2009). Earthquake focal mechanisms of the induced seismicity in 2006 and 2007 below basel (switzerland). *Swiss Journal of Geosciences*, *102*(3), 457. Retrieved from https://doi.org/10.1007/s00015-009-1336-y doi: 10.1007/s00015-009-1336-y

Eaton, D. W., Igonin, N., Poulin, A., Weir, R., Zhang, H., Pellegrino, S., & Rodriguez, G. (2018). Induced seismicity characterization during hydraulic-fracture monitoring with a shallow-wellbore geophone array and broadband sensors. *Seismological Research Letters*, *89*(5), 1641–1651. Retrieved from https://doi.org/10.1785/0220180055 doi: 10.1785/0220180055

Ford, A., Blenkinsop, T., & Mclellan, J. (2009). Factors affecting fluid flow in strike-slip fault systems: coupled deformation and fluid flow modelling with application to the western mount isa inlier, australia. *Geofluids*, *9*(1), 2–23. doi: 10.1111/j.1468-8123.2008.00219.x

Giorgetti, C., Carpenter, B. M., & Collettini, C. (2015). Frictional behavior of talc-calcite mixtures. *Journal of Geophysical Research: Solid Earth*, *120*(9), 6614-6633. Retrieved from https://agupubs.onlinelibrary.wiley.com/doi/abs/10.1002/2015JB011970 doi: https://doi.org/10.1002/2015JB011970

Han, J., Kim, S., & Sheen, D. (2025, 02). Rpnet: Robust p-wave first-motion polarity determination using deep learning. *Seismological Research Letters*, *96*(4), 2405-2417. Retrieved from https://doi.org/10.1785/0220240384 doi: 10.1785/0220240384

Hassani, A., Walton, S., Shah, N., Abuduweili, A., Li, J., & Shi, H. (2021). Escaping the big data paradigm with compact transformers. *arXiv preprint arXiv:2104.05704*.

Hendrycks, D., & Gimpel, K. (2016). Gaussian error linear units (gelus). *arXiv preprint arXiv:1606.08415*.

Igonin, N., Verdon, J. P., Kendall, J.-M., & Eaton, D. W. (2021). Large-scale fracture systems are permeable pathways for fault activation during hydraulic fracturing. *Journal of Geophysical Research: Solid Earth*, *126*(3), e2020JB020311. Retrieved from https://agupubs.onlinelibrary.wiley.com/doi/abs/10.1029/2020JB020311 (e2020JB020311 2020JB020311) doi: https://doi.org/10.1029/2020JB020311

Ioffe, S. (2015). Batch normalization: Accelerating deep network training by reducing internal covariate shift. *arXiv preprint arXiv:1502.03167*.

Jia, S. Q., Eaton, D. W., & Wong, R. C. (2018, 07). Stress inversion of shear-tensile focal mechanisms with application to hydraulic fracture monitoring. *Geophysical Journal International*, *215*(1), 546-563. Retrieved from https://doi.org/

10.1093/gji/ggy290 doi: 10.1093/gji/ggy290

Kagan, Y. Y. (1991, 09). 3-d rotation of double-couple earthquake sources. *Geophysical Journal International*, *106*(3), 709-716. Retrieved from https://doi.org/10.1111/j.1365-246X.1991.tb06343.x doi: 10.1111/j.1365-246X.1991.tb06343.x

Kamei, R., Nakata, N., & Lumley, D. (2015). Introduction to microseismic source mechanisms. *The Leading Edge*, *34*, 876–878, 880. doi: 10.1190/tle34080876.1

Kim, Y., Liu, Q., & Tromp, J. (2011, 07). Adjoint centroid-moment tensor inversions. *Geophysical Journal International*, *186*(1), 264-278. Retrieved from https://doi.org/10.1111/j.1365-246X.2011.05027.x doi: 10.1111/j.1365-246X.2011.05027.x

Kingma, D. P., & Ba, J. (2017). *Adam: A method for stochastic optimization.* Retrieved from https://arxiv.org/abs/1412.6980

Kuang, W., Yuan, C., & Zhang, J. (2021). Real-time determination of earthquake focal mechanism via deep learning. *Nature Communications*, *12*(1), 1432. Retrieved from https://doi.org/10.1038/s41467-021-21670-x doi: 10.1038/s41467-021-21670-x

Lapins, S., Goitom, B., Kendall, J.-M., Werner, M. J., Cashman, K. V., & Hammond, J. O. S. (2021). A little data goes a long way: Automating seismic phase arrival picking at nabro volcano with transfer learning. *Journal of Geophysical Research: Solid Earth*, *126*(7), e2021JB021910. Retrieved from https://agupubs.onlinelibrary.wiley.com/doi/abs/10.1029/2021JB021910 (e2021JB021910 2021JB021910) doi: https://doi.org/10.1029/2021JB021910

Li, B. Q. (2025). Pore pressure inhibits clustering of induced earthquakes in western canada. *Proceedings of the National Academy of Sciences*, *122*(2), e2407345121. Retrieved from https://www.pnas.org/doi/abs/10.1073/pnas.2407345121 doi: 10.1073/pnas.2407345121

Li, C., Saad, O. M., & Chen, Y. (2025). Unsupervised deep learning for off-the-grid seismic reconstruction and denoising. *GEOPHYSICS*, *90*(3), V241-V254. Retrieved from https://doi.org/10.1190/geo2024-0189.1 doi: 10.1190/geo2024-0189.1

Loshchilov, I., & Hutter, F. (2016). Sgdr: Stochastic gradient descent with warm restarts. *arXiv preprint arXiv:1608.03983*.

McKenzie, D. P. (1969, 04). The relation between fault plane solutions for earthquakes and the directions of the principal stresses. *Bulletin of the Seismological Society of America*, *59*(2), 591-601. Retrieved from https://doi.org/10.1785/BSSA0590020591 doi: 10.1785/BSSA0590020591

Meng, H., & Ben-Zion, Y. (2017, 09). Detection of small earthquakes with dense array data: example from the san jacinto fault zone, southern california. *Geophysical Journal International*, *212*(1), 442-457. Retrieved from https://doi.org/10.1093/gji/ggx404 doi: 10.1093/gji/ggx404

Mousavi, S. M., & Beroza, G. C. (2020). A machine-learning approach for earthquake magnitude estimation. *Geophysical Research Letters*, *47*, e2019GL085976. doi: 10.1029/2019GL085976

Mousavi, S. M., Ellsworth, W. L., Zhu, W., Chuang, L. Y., & Beroza, G. C. (2020). Earthquake transformer—an attentive deep-learning model for simultaneous earthquake detection and phase picking. *Nature Communications*, *11*, 3952. doi: 10.1038/s41467-020-17591-w

Niksejel, A., & Zhang, M. (2024, 02). Obstransformer: a deep-learning seismic phase picker for obs data using automated labelling and transfer learning. *Geophysical Journal International*, *237*(1), 485-505. Retrieved from https://doi.org/10.1093/gji/ggae049 doi: 10.1093/gji/ggae049

Nyffenegger, P. A., Tinker, M. A., Zhang, J., Grant, E. B., Hutchenson, K. D., & Lawton, D. C. (2022). Compact phased arrays for microseismic monitor-

ing [Journal Article]. *First Break*, *40*(4), 69-74. Retrieved from https://www.earthdoc.org/content/journals/10.3997/1365-2397.fb2022033 doi: https://doi.org/10.3997/1365-2397.fb2022033

Perol, T., Gharbi, M., & Denolle, M. (2018). Convolutional neural network for earthquake detection and location. *Science Advances*, *4*(2), e1700578. doi: 10.1126/sciadv.1700578

Reches, Z., Baer, G., & Hatzor, Y. (1992). Constraints on the strength of the upper crust from stress inversion of fault slip data. *Journal of Geophysical Research*, *97*, 12481–12493. doi: 10.1029/90JB02258

Ross, Z. E., Meier, M.-A., & Hauksson, E. (2018). P wave arrival picking and first-motion polarity determination with deep learning. *Journal of Geophysical Research: Solid Earth*, *123*(6), 5120–5143. Retrieved from https://doi.org/10.1029/2017JB015251 doi: 10.1029/2017JB015251

Ross, Z. E., Meier, M. A., Hauksson, E., & Heaton, T. H. (2018). Generalized seismic phase detection with deep learning. *Bulletin of the Seismological Society of America*, *108*(5A), 2894–2901. doi: 10.1785/0120180080

Ross, Z. E., Yue, Y., Meier, M.-A., Hauksson, E., & Heaton, T. H. (2019). Phaselink: A deep learning approach to seismic phase association. *Journal of Geophysical Research: Solid Earth*, *124*(1), 856-869. Retrieved from https://agupubs.onlinelibrary.wiley.com/doi/abs/10.1029/2018JB016674 doi: https://doi.org/10.1029/2018JB016674

Saad, O. M., & Chen, Y. (2020). Earthquake detection and p-wave arrival time picking using capsule neural network. *IEEE Transactions on Geoscience and Remote Sensing*, *59*(7), 6234–6243. doi: 10.1109/tgrs.2020.3019520

Saad, O. M., & Chen, Y. (2021). Capsphase: Capsule neural network for seismic phase classification and picking. *IEEE Transactions on Geoscience and Remote Sensing*, *60*, 1–11. doi: 10.1109/tgrs.2021.3089929

Saad, O. M., Chen, Y., Savvaidis, A., Fomel, S., & Chen, Y. (2022). Real-time earthquake detection and magnitude estimation using vision transformer. *Journal of Geophysical Research: Solid Earth*, *127*(5), e2021JB023657. doi: 10.1029/2021jb023657

Saad, O. M., Chen, Y., Siervo, D., Zhang, F., Savvaidis, A., Huang, G.-c. D., ... Chen, Y. (2023). Eqcct: A production-ready earthquake detection and phase-picking method using the compact convolutional transformer. *IEEE Transactions on Geoscience and Remote Sensing*, *61*, 1-15. doi: 10.1109/TGRS.2023.3319440

Saad, O. M., Ravasi, M., & Alkhalifah, T. (2025). Self-supervised multi-stage deep learning network for seismic data denoising. *Artificial Intelligence in Geosciences*, *6*(1), 100123. Retrieved from https://www.sciencedirect.com/science/article/pii/S266654412500019X doi: https://doi.org/10.1016/j.aiig.2025.100123

Saad, O. M., Savvaidis, A., & Chen, Y. (2024). Transfer learning for seismic phase picking with significantly higher precision in faraway seismic stations. *IEEE Transactions on Geoscience and Remote Sensing*, *62*, 1-12. doi: 10.1109/TGRS.2024.3422612

Sagy, A., Brodsky, E. E., & Axen, G. J. (2007, 03). Evolution of fault-surface roughness with slip. *Geology*, *35*(3), 283-286. Retrieved from https://doi.org/10.1130/G23235A.1 doi: 10.1130/G23235A.1

Scholz, C. H. (1987, 06). Wear and gouge formation in brittle faulting. *Geology*, *15*(6), 493-495. Retrieved from https://doi.org/10.1130/0091-7613(1987)15<493:WAGFIB>2.0.CO;2 doi: 10.1130/0091-7613(1987)15⟨493:WAGFIB⟩2.0.CO;2

Shen, L. W., Schmitt, D. R., & Haug, K. (2019). Quantitative constraints to the complete state of stress from the combined borehole and focal mechanism inversions: Fox creek, alberta. *Tectonophysics*, *764*, 110-123. Re-

trieved from https://www.sciencedirect.com/science/article/pii/S0040195119301477 doi: https://doi.org/10.1016/j.tecto.2019.04.023

Skoumal, R. J., Hardebeck, J. L., & Michael, A. J. (in review). pysatsi: A python package for computing focal mechanism stress inversions. *Seismological Research Letters*. (in review)

Skoumal, R. J., Hardebeck, J. L., & Shearer, P. M. (2024, 04). Skhash: A python package for computing earthquake focal mechanisms. *Seismological Research Letters*, *95*(4), 2519-2526. Retrieved from https://doi.org/10.1785/0220230329 doi: 10.1785/0220230329

Southern California Earthquake Data Center. (2013). *Southern California Earthquake Data Center.* California Institute of Technology, Dataset. Retrieved from https://doi.org/10.7909/C3WD3xH1 doi: 10.7909/C3WD3xH1

Tape, W., & Tape, C. (2012, 11). Angle between principal axis triples. *Geophysical Journal International*, *191*(2), 813-831. Retrieved from https://doi.org/10.1111/j.1365-246X.2012.05658.x doi: 10.1111/j.1365-246X.2012.05658.x

Terakawa, T., Miller, S. A., & Deichmann, N. (2012). High fluid pressure and triggered earthquakes in the enhanced geothermal system in basel, switzerland. *Journal of Geophysical Research: Solid Earth*, *117*(B7). Retrieved from https://agupubs.onlinelibrary.wiley.com/doi/abs/10.1029/2011JB008980 doi: https://doi.org/10.1029/2011JB008980

Tian, X., Chen, Y., Zhang, X., Zhang, W., & Wang, X. (2025, 01). Focal mechanism determination by location-constrained deep learning: Application to microseismic monitoring. *Geophysics*, *90*(2), L31-L42. Retrieved from https://doi.org/10.1190/geo2024-0478.1 doi: 10.1190/geo2024-0478.1

Trow, A. J., Zhang, H., Record, A. S., Mendoza, K. A., Pankow, K. L., & Wannamaker, P. E. (2018, 07). Microseismic event detection using multiple geophone arrays in southwestern utah. *Seismological Research Letters*, *89*(5), 1660-1670. Retrieved from https://doi.org/10.1785/0220180065 doi: 10.1785/0220180065

Uchide, T. (2020). Focal mechanisms of small earthquakes beneath the japanese islands based on first-motion polarities picked using deep learning. *Geophysical Journal International*, *223*, 1658–1671. doi: 10.1093/gji/ggaa401

Van den Ende, M. P., & Ampuero, J. P. (2020). Automated seismic source characterization using deep graph neural networks. *Geophysical Research Letters*, *47*(17), e2020GL088690. doi: 10.1029/2020gl088690

van der Baan, M., Eaton, D., & Dusseault, M. (2013). Microseismic monitoring developments in hydraulic fracture stimulation. In A. P. Bunger, J. McLennan, & R. Jeffrey (Eds.), *Effective and sustainable hydraulic fracturing* (chap. 21). Rijeka: IntechOpen. Retrieved from https://doi.org/10.5772/56444 doi: 10.5772/56444

Vaswani, A. (2017). Attention is all you need. *Advances in Neural Information Processing Systems*.

Wang, J., Xiao, Z., Liu, C., Zhao, D., & Yao, Z. (2019). Deep learning for picking seismic arrival times. *Journal of Geophysical Research: Solid Earth*, *124*(7), 6612–6624. doi: 10.1029/2019JB017536

Wang, P., Ren, T., Shen, R., Chen, H., Liu, X., & Meng, F. (2024). Determination of earthquake focal mechanism via multi-task learning. *Computers Geosciences*, *184*, 105513. Retrieved from https://www.sciencedirect.com/science/article/pii/S0098300423002170 doi: https://doi.org/10.1016/j.cageo.2023.105513

Weir, R. M., Eaton, D. W., Eyre, T. S., & Lawton, D. C. (2022). Integrated interpretation: Defining risk corridors by combining 3-d seismic interpretation with induced seismicity hypocenters. *Tectonophysics*, *827*, 229263. Retrieved from https://www.sciencedirect.com/science/article/pii/S0040195122000579 doi: https://doi.org/10.1016/j.tecto.2022.229263

Yang, L., & Wang, R. (2024, 12). Nandc: Full moment tensor inversion and uncertainty analysis for large-n monitored small earthquakes. *Seismological Research Letters*. Retrieved from https://doi.org/10.1785/0220240219 doi: 10.1785/0220240219

Yu, S., & Ma, J. (2021). Deep learning for geophysics: Current and future trends. *Reviews of Geophysics*, *59*(3), e2021RG000742. Retrieved from https://agupubs.onlinelibrary.wiley.com/doi/abs/10.1029/2021RG000742 (e2021RG000742 2021RG000742) doi: https://doi.org/10.1029/2021RG000742

Zhang, C., Fan, D., Elsworth, D., He, M., Zhao, X., Zhu, C., & Zhang, H. (2024). Mechanisms of stress- and fluid-pressure-driven fault reactivation in gonghe granite: Implications for injection-induced earthquakes. *International Journal of Rock Mechanics and Mining Sciences*, *174*, 105642. Retrieved from https://www.sciencedirect.com/science/article/pii/S1365160924000078 doi: https://doi.org/10.1016/j.ijrmms.2024.105642

Zhang, F., Wang, R., Chen, Y., & Chen, Y. (2022, 08). Spatiotemporal variations in earthquake triggering mechanisms during multistage hydraulic fracturing in western canada. *Journal of Geophysical Research: Solid Earth*, *127*. doi: 10.1029/2022JB024744

Zhang, H., Eaton, D. W., Rodriguez, G., & Jia, S. Q. (2019, 03). Source-mechanism analysis and stress inversion for hydraulic-fracturing-induced event sequences near fox creek, alberta. *Bulletin of the Seismological Society of America*, *109*(2), 636-651. Retrieved from https://doi.org/10.1785/0120180275 doi: 10.1785/0120180275

Zhang, M., Liu, M., Feng, T., Wang, R., & Zhu, W. (2022). Loc-flow: An end-to-end machine learning-based high-precision earthquake location workflow. *Seismological Research Letters*, *93*, 2426–2438. doi: 10.1785/0220220019

Zhang, X., Zhang, M., & Tian, X. (2021). Real-time earthquake early warning with deep learning: Application to the 2016 m 6.0 central apennines, italy earthquake. *Geophysical Research Letters*, *48*(5), e2020GL089394. doi: 10.1029/2020gl089394

Zhao, M., Xiao, Z., Zhang, M., Yang, Y., Tang, L., & Chen, S. (2023). Diting-motion: A deep-learning first-motion-polarity classifier and its application to focal mechanism inversion. *Frontiers in Earth Science*, *11*, 1103914. doi: 10.3389/feart.2023.1103914

Zhou, Y., Yue, H., Zhou, S., & Kong, Q. (2019). Hybrid event detection and phase-picking algorithm using convolutional and recurrent neural networks. *Seismological Research Letters*, *90*(3), 1079–1087. doi: 10.1785/0220180319

Zhu, W., & Beroza, G. C. (2018, 10). Phasenet: a deep-neural-network-based seismic arrival-time picking method. *Geophysical Journal International*, *216*(1), 261-273. Retrieved from https://doi.org/10.1093/gji/ggy423 doi: 10.1093/gji/ggy423

Zhu, W., Mousavi, S. M., & Beroza, G. C. (2019). Seismic signal denoising and decomposition using deep neural networks. *IEEE Transactions on Geoscience and Remote Sensing*, *57*(11), 9476–9488. doi: 10.1109/tgrs.2019.2926772

Zhu, W., Song, J., Wang, H., & Münchmeyer, J. (2025). *Towards end-to-end earthquake monitoring using a multitask deep learning model.* Retrieved from https://arxiv.org/abs/2506.06939

Zoback, M. L. (1992). First- and second-order patterns of stress in the lithosphere: The world stress map project. *Journal of Geophysical Research: Solid Earth*, *97*(B8), 11703-11728. Retrieved from https://agupubs.onlinelibrary.wiley.com/doi/abs/10.1029/92JB00132 doi: https://doi.org/10.1029/92JB00132

Supporting Information for "Massive High-Fidelity Focal Mechanisms Reveal Detailed Structure of Re-Activated Faults During Hydraulic Fracturing in Western Canada"

Jiachen Hu[1], Yunfeng Chen[1], Hongyu Yu[1], Fangxue Zhang[1], Xing Li[2],

Yangkang Chen[2]

[1]Key Laboratory of Geoscience Big Data and Deep Resource of Zhejiang Province, Zhejiang University, Hangzhou 310027, Zhejiang, China

[2]Bureau of Economic Geology, The University of Texas at Austin, University Station, Box X Austin, Texas 78713-8924

September 14, 2025, 11:41am

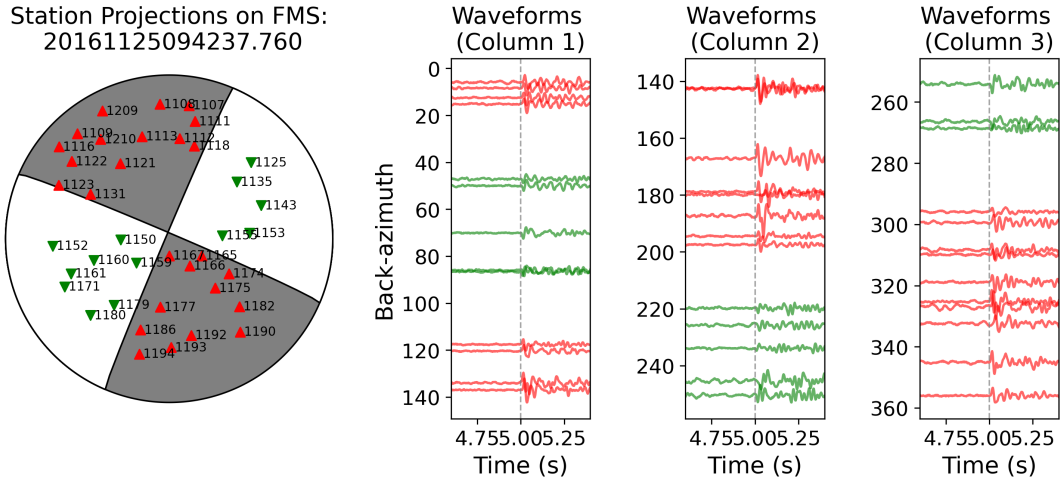

Figure S1. Strike-slip fault combining station projections with corresponding waveforms. The left panel displays a focal mechanism where red upward triangles indicate stations recording upward polarities and green downward triangles show downward polarities. The right panels present waveform data from 4.6-5.4s, with red and green traces matching their corresponding station polarities, arranged azimuthally from top to bottom and left to right.